ACS NANO

www.acsnano.org

ARTICLE

Artificial Intelligence-Guided Cancer Engineering for Tumor Normalization Executed by Tumor Lysosomal-Triggered Supramolecular Chiral Peptide

Jingmei Wang, Weiming You, Wangxiao He,*,∇ Jin Yan,*,∇ and Yanmin Zhang*,∇

Cite This: *ACS Nano* 2025, 19, 17273−17286

Read Online

ACCESS | Metrics & More | Article Recommendations | Supporting Information

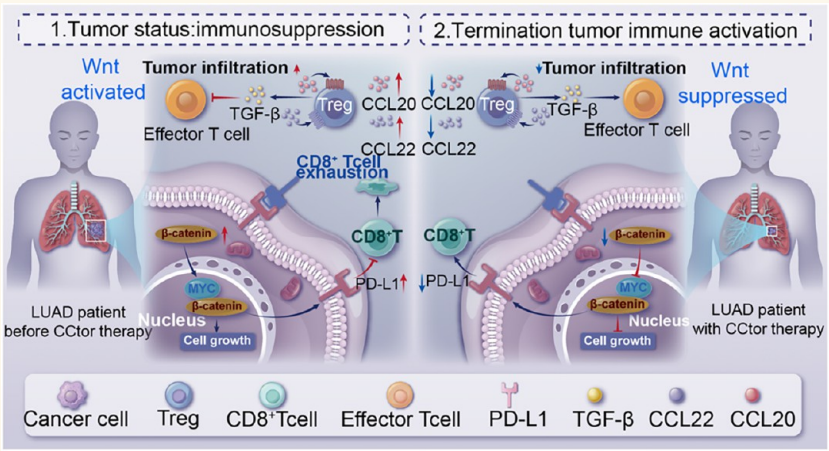

ABSTRACT: **Cancer engineering for tumor normalization offers a promising therapeutic strategy to reverse malignant cells and their supportive tumor microenvironment into a more benign state. Herein, an artificial intelligence (AI) approach was developed using mRNA data from patients with lung adenocarcinoma to facilitate the identification of aberrant signaling pathways, specifically focusing on PD-L1, Wnt, and macropinocytosis. Targeting these characteristics, we have developed a supramolecular construct called cancer corrector (CCtor) with the aim of harnessing the enhanced macropinocytosis observed in cancer cells. Undergoing cleavage and subsequent drug release triggered by the lysosomal protease in cancer cells, CCtor rectifies the aberrant hyperactivity of both Wnt and PD-L1 signaling pathways. This dual-action therapeutic strategy not only restores normalcy to cancer cells but also exerts an exceptionally robust therapeutic effect. This work exemplifies a future direction for cancer therapies by combining AI with molecular engineering to significantly improve patient outcomes through tumor behavior normalization.**

KEYWORDS: *cancer engineering, tumor normalization, antitumor immunity, cancer therapy, LUAD*

INTRODUCTION

The intricate nature of cancer manifests through unbridled alterations and mutations in its genome, epigenome, and microenvironment, as well as aberrations stemming from disruptions to cellular processes that are meticulously regulated during normal development and wound repair.[1,2] A growing body of research has identified the dynamic interplay between tumor cells and their surrounding microenvironment, collectively known as the tumor microenvironment (TME), as a critical factor in cancer progression and therapeutic resistance.[3,4]

The innovative concept of tumor normalization seeks to revert malignant cells and their supportive TME to a more benign

Received: October 10, 2024
Revised: April 4, 2025
Accepted: April 22, 2025
Published: April 29, 2025

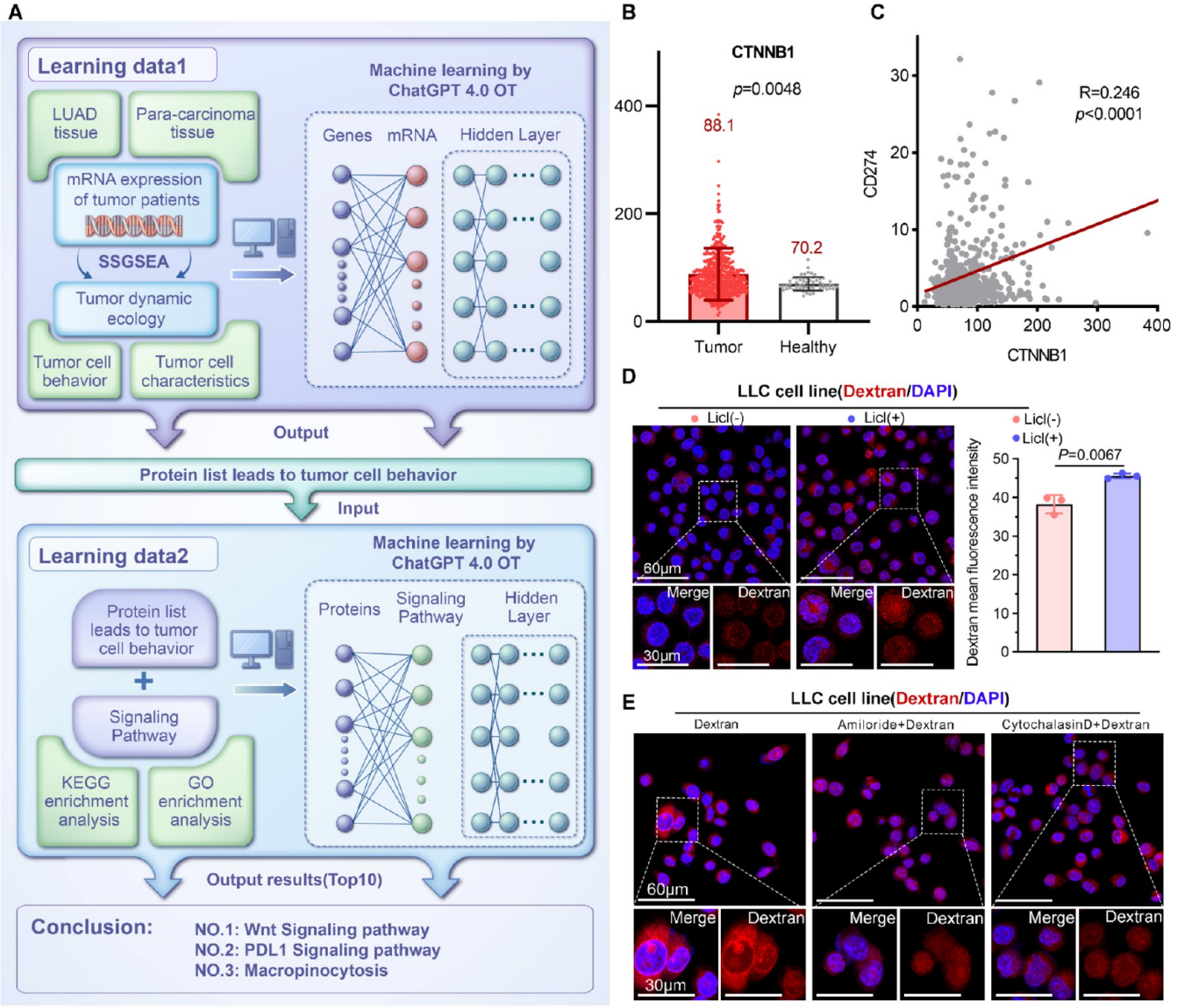

Figure 1. Identifying Key Aberrant Signaling Pathways in LUAD Using AI. (A) Flowchart of artificial intelligence analysis of NSCLC disease models. (B) Differential analysis of CTNNB1 expression between tumor group and healthy group. (C) The CTNNB1 expression was positively correlated with CD274 in LUAD tumor group. (D) Representative images of LSCM and quantification statistics of TRITC-dextran fluorescence intensity incubating with/without the Wnt activator Licl for LLC cell line (n = 3). P values were calculated by the independent sample t test. (E) Representative images of LSCM of TRITC-dextran fluorescence intensity incubating with/without the macropinocytosis inhibitors (Amiloride and Cytochalasin D) for LLC cell line (n = 3).

state, offering a promising therapeutic approach that transcends the limitations of conventional chemotherapy and radiotherapy.[5−7] Tumor normalization encompasses two principal strategies: the normalization of tumor cells and the normalization of the TME.[8−10] Clinically, this paradigm has demonstrated remarkable outcomes, exemplified by differentiation therapy, which has achieved remission in certain leukemias by inducing malignant cells to mature into non-proliferative forms.[11,12] Compared to traditional treatments, tumor normalization targets the root mechanisms of malignancy, potentially minimizing side effects and overcoming resistance.[13,14]

The hallmark of tumor cells lies in their aberrant signaling pathways, distinguishing them from normal cells.[15−18] Correcting these dysregulated pathways is fundamental to achieving tumor normalization.[19−21] However, the challenge lies in accurately identifying these abnormal signals and designing effective corrective measures.[22,23] Current bioinformatics analyses, while valuable, often fall short in terms of precision and speed, highlighting a significant area for improvement.[24,25] In this context, artificial intelligence (AI) emerges as a revolutionary tool, offering the potential to rapidly and accurately identify aberrant tumor signals, thus paving the way for advanced cancer therapies.[26,27]

With a focus on lung adenocarcinoma (LUAD) as a proof-of-concept, we utilized single-sample Gene Set Enrichment Analysis (ssGSEA) to transform mRNA data from patients into comprehensive scores that encompass diverse characteristics of tumor malignancy, including proliferation, metastasis, invasion, and immune evasion.[28] Additionally, we incorporated features of the tumor microenvironment such as immune cell infiltration and activity.[29] Leveraging the capabilities of

https://doi.org/10.1021/acsnano.4c14264
ACS Nano 2025, 19, 17273−17286

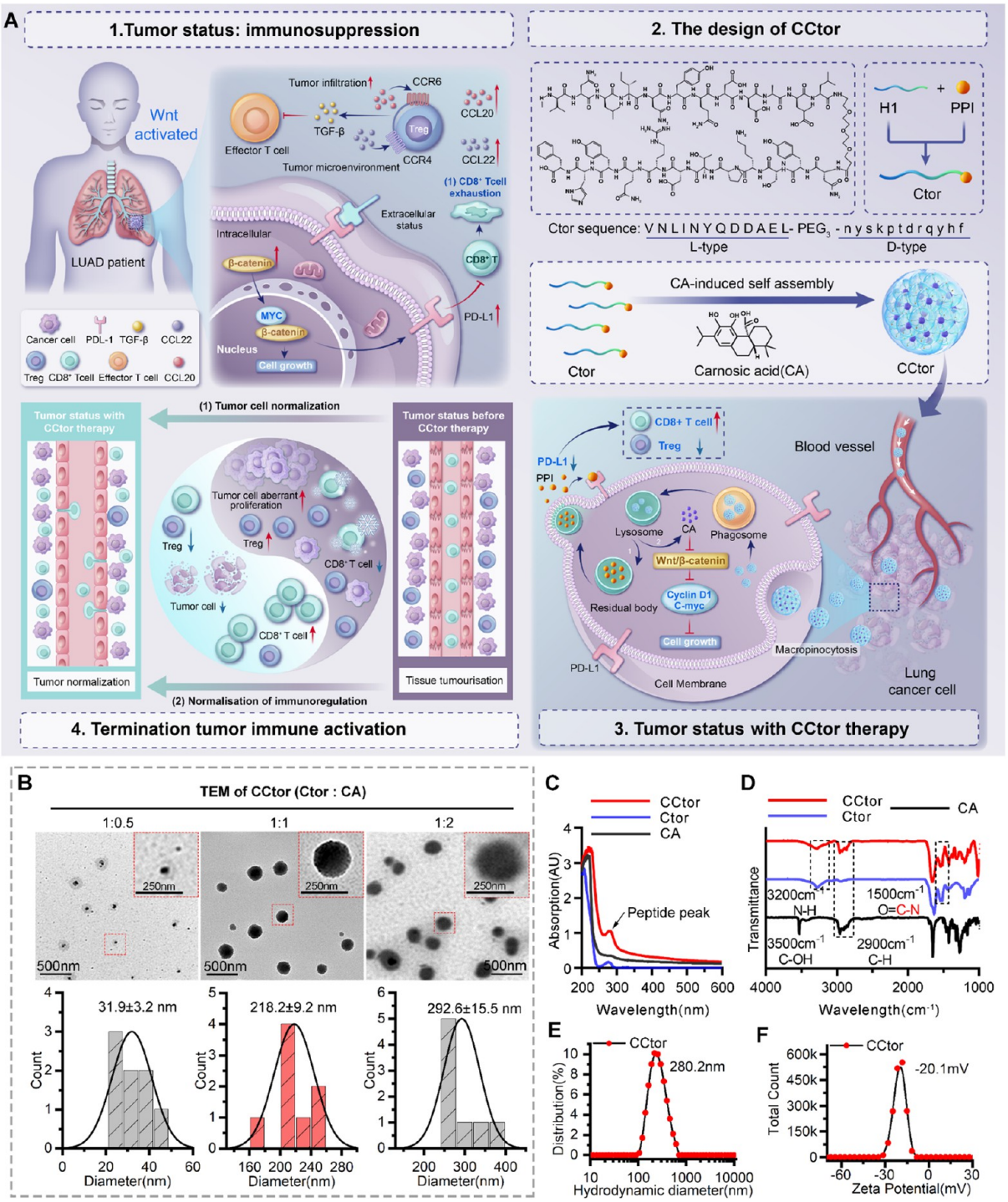

Figure 2. Design, synthesis and characterization of CCtor, a promising immune checkpoint inhibitor. (A) Schematic representation of the therapeutic strategy of CCtor against resistance to PD-1/PD-L1 checkpoint blockade therapy for lung adenocarcinoma (LUAD) patients, which enhances CD8$^+$ T cell proliferation by inhibiting the active Wnt/β-catenin signaling pathway and reducing intratumoral infiltration of regulatory T cells (Tregs). (B) TEM images of CCtor were induced by different concentrations of CA (0.5, 1, and 2 mg/mL). The Histograms of corresponding particles size distribution of CCtor were respectively counted at the different concentrations of CA. (C) UV spectra of Ctor, CA, and CCtor (Ctor: CA = 1). The typical absorption peak of the peptide was marked with a black arrow. (D) Fourier-transform infrared spectroscopy (FTIR) of Ctor, CA, and CCtor (Ctor: CA = 1). Two absorption peaks at 3200 and 1500 cm^{-1} were attributed to the peptide's stretching vibration N−H and C−N. Two absorption peaks at 3500 and 2900 cm^{-1} were distributed to the stretching vibration C−OH and C−H of CA. (E) The hydrodynamic diameter of CCtor (Ctor: CA = 1) was measured by DLS. (F) The ζ-potential of CCtor (Ctor: CA = 1) was measured in distilled water at pH 6.5.

ChatGPT, we have developed an analytical tool herein that integrates ssGSEA results with mRNA data to pinpoint the signaling pathways most closely associated with malignant behaviors, effectively distinguishing tumor tissues from normal ones. Our analysis has identified the PD-L1 pathway, Wnt signaling and macropinocytosis as the primary drivers of

https://doi.org/10.1021/acsnano.4c14264
ACS Nano 2025, 19, 17273−17286

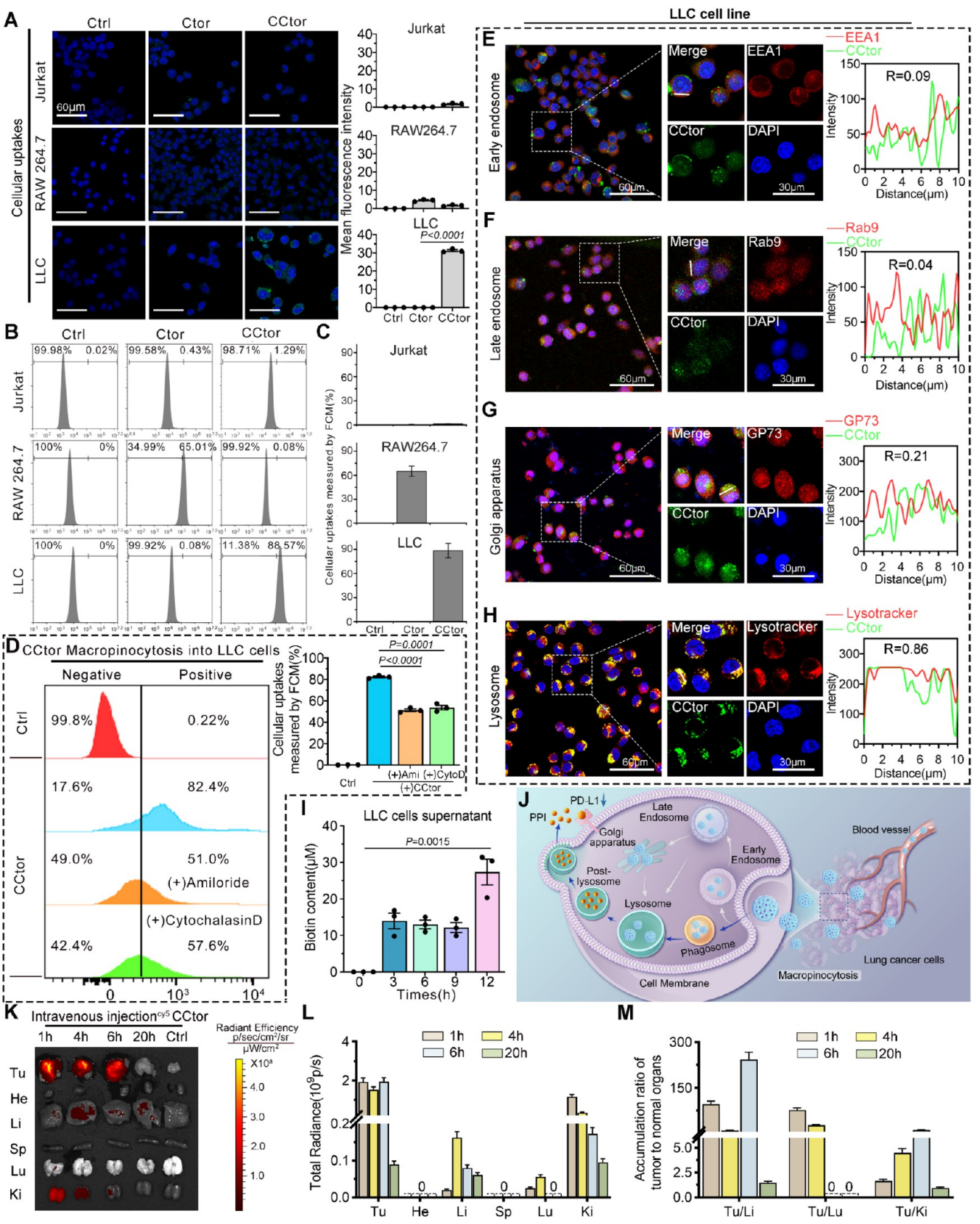

Figure 3. CCtor exhibited excellent selectivity in internalizing tumor cells via macropinocytosis. (A) Representative confocal images and mean fluorescence intensity of FITC-Ctor and FITC−CCtor cellular uptakes into LLC, Raw264.7 and Jurkat cells, respectively. Scale bar: 60 μm. (B, C) The quantifies determination and analysis of FITC-Ctor and FITC−CCtor cellular uptakes into cells by single-channel flow cytometry. (D) FCM analysis and quantitative statistics of CCtor cellular uptakes of into LLC cells. (E−H) Co-localization of FITC−CCtor and EEA1 (Early endosome marker) (E), FITC−CCtor and Rab9 (Late endosome marker) (F), FITC−CCtor and GP73 (golgi apparatus membrane protein)

https://doi.org/10.1021/acsnano.4c14264
ACS Nano 2025, 19, 17273−17286

Figure 3. continued

(G), FITC−CCtor and lysotracker (Lysosome Probe) (H) in LLC cells. The Pearson confocal coefficient (PCC) was used to quantify the degree of colocalization. (I) The content of biotin was detected in LLC cells supernatants by colorimetric biotin assay kit. The escape mechanisms depiction for CCtor in the golgi apparatus and endosomes. (J) Schematic representation of CCtor was uptake by tumor cells by micropinocytosis and degraded via the lysosomal pathway. (K) Drug distribution in main organs of C57BL/6 mice bearing LLC tumors after 0, 1, 4, 6, and 20 h intravenous injection of cy5-labelled CCtor. (L, M) Quantitative statistics of the total fluorescence intensity (L) and tumor-to-normal tissue ratios (M) for cy5-labelled CCtor intravenous injection after 0, 1, 4, 6, and 20 h.

malignancy in LUAD. Building upon these profound insights, we have ingeniously devised a supramolecular construct known as cancer corrector (CCtor), which elegantly infiltrates tumor cells via macropinocytosis and is subsequently transported to the lysosome. Within this intracellular compartment, CCtor undergoes degradation in response to the overexpression of lysosomal protease specifically observed in cancer cells. This orchestrated disintegration liberates a potent Wnt inhibitor (CA) alongside a PD-L1 antagonist peptide (PPI), thereby rectifying the aberrant hyperactivity of both Wnt and PD-L1 signaling pathways. Remarkably, this dual-action therapeutic strategy not only restores normalcy to lung cancer cells but also exerts an exceptionally robust therapeutic effect. The significance of this study transcends its immediate clinical implications, as it establishes a comprehensive model for tumor normalization therapy that seamlessly integrates AI-driven identification of critical aberrant signaling pathways with targeted interventions to rectify these abnormalities. This groundbreaking model heralds a paradigm shift in cancer treatment, offering an avenue to achieve tumor normalization and enhance patient outcomes through the meticulous fusion of advanced computational techniques and innovative therapeutic design.

RESULTS AND DISCUSSION

Identifying Key Aberrant Signaling Pathways in LUAD Using AI. Researchers initially downloaded mRNA expression data from TCGA for 59 normal lung tissues and 515 LUAD lung cancer tissues. These data were analyzed using ssGSEA to evaluate critical cancer pathways and immune cell infiltration pathways (Figure S1). The results were then fed into ChatGPT 4OT, which analyzed the data and identified the gene sets contributing most significantly to cancer behavior in malignant tissues compared to normal tissues (Figure 1A). Further analysis using ChatGPT 4OT identified the most frequently activated signaling pathways in the cancerous tissues. Two AI assessments revealed that the key aberrantly activated signaling pathways in tumor tissues were the Wnt signaling, PD-L1 signaling, and macropinocytosis pathways (Figure 1A).

Furthermore, the mRNA expression level of CTNNB1 (β-catenin), a pivotal protein in the Wnt signaling pathway, exhibited significantly elevated levels in tumor tissues compared to healthy tissue in LUAD (Figure 1B), thereby corroborating the findings derived from AI analysis. Additionally, there was a statistically significant positive correlation observed between CD274 (PD-L1) mRNA expression and CTNNB1 levels (Figure 1C). Similar results were confirmed in macropinocytosis, where the mRNA expression levels of key proteins involved in its regulation were significantly elevated in cancerous tissues compared to healthy tissues (Figure S2A). Moreover, there was a significant positive correlation between the mRNA expression levels of these key regulatory proteins (particularly RAC1, CDC42, RAB5A, PIK3CA, EEA1, PAK1 and KRAS) and the expression level of CTNNB1 (Figure S2B). Additionally, it was discovered that lithium chloride, an activator of the Wnt signaling pathway, effectively augmented dextran uptake in LLC, PC-9 and erlotinib-resistant PC-9 lung adenocarcinoma cells, thus indicating further activation of the macropinocytosis pathway (Figures 1D and S2C,D). Finally, overexpression of β-catenin in LLC lung adenocarcinoma cells confirmed that activation of the Wnt/β-catenin pathway significantly enhances cellular macropinocytosis activity (Figure S2E,F). This observation was further substantiated by demonstrating that inhibitors of macropinocytosis such as Amiloride and Cytochalasin D impeded dextran uptake (Figure 1E). These findings indicate that macropinocytosis is activated in tumor cells, and this activation is dependent on the Wnt pathway, potentially facilitating nutrient acquisition for cancer cells. Collectively, these results further substantiate the AI driven discoveries that the key signaling pathways aberrantly activated in tumor tissues include Wnt signaling, PD-1 signaling, and macropinocytosis pathways.

Design, Synthesis, and Characterization of CCtor. Inspired by these clinical data analysis results, researchers hypothesized that concurrently correcting the aberrant activation of the Wnt and PD-1/PD-L1 pathways in LUAD patients could normalize tumor cells, thereby achieving tumor treatment. Additionally, the tumor-specific increase in macropinocytosis could be exploited for tumor-specific targeting of therapeutic molecules (Figure 2A). Given that macropinocytosis is an effective pathway for the internalization of soluble proteins, it was proposed to coassemble a previously developed Wnt pathway inhibitor CA with a D-type PD-L1 antagonist peptide (PPI) into a protein-like particle, named CCtor. For this assembly, the CA-induced polymerizing H1 sequence was linked to the C-terminus of PPI, leveraging the CA-induced polymerization to construct the protein-like particle CCtor (Figure 2A). Once internalized by tumor cells, the lysosomal degradation of the L-type polypeptide part of CCtor would release CA and the D-type dodecapeptide PPI, allowing CA to enter the cytoplasm and PPI to function extracellularly by binding to PD-L1 (Figure 2A).

To achieve this design, the polypeptide Ctor linking H1 and PPI was synthesized using solid-phase synthesis, purified using reverse-phase chromatography, and characterized for purity and molecular structure by LC-MS (Figure S3A). The supramolecular assembly of CCtor was constructed in a one-pot process induced by CA, with the particle size tunable by varying the Ctor ratio (Figure 2B). Transmission electron microscopy (TEM) observations showed uniform particle size with a diameter of about 218.2 nm at a Ctor mass ratio of 1:1. To ensure better penetration in tumor tissues, an equal ratio (Ctor = 1:1) was adopted for subsequent work. Furthermore, TEM also observations revealed that in the absence of the L-type H1 peptide (Sequence: VNLINYQDDAEL), the particles formed through the self-assembly of D-type PPI peptide and CA were sparse and irregular (Figure S4A). This finding was consistent with previous studies, suggesting that the L-type H1 peptide facilitates CA self-assembly. To further investigate the effect of

https://doi.org/10.1021/acsnano.4c14264
ACS Nano 2025, 19, 17273−17286

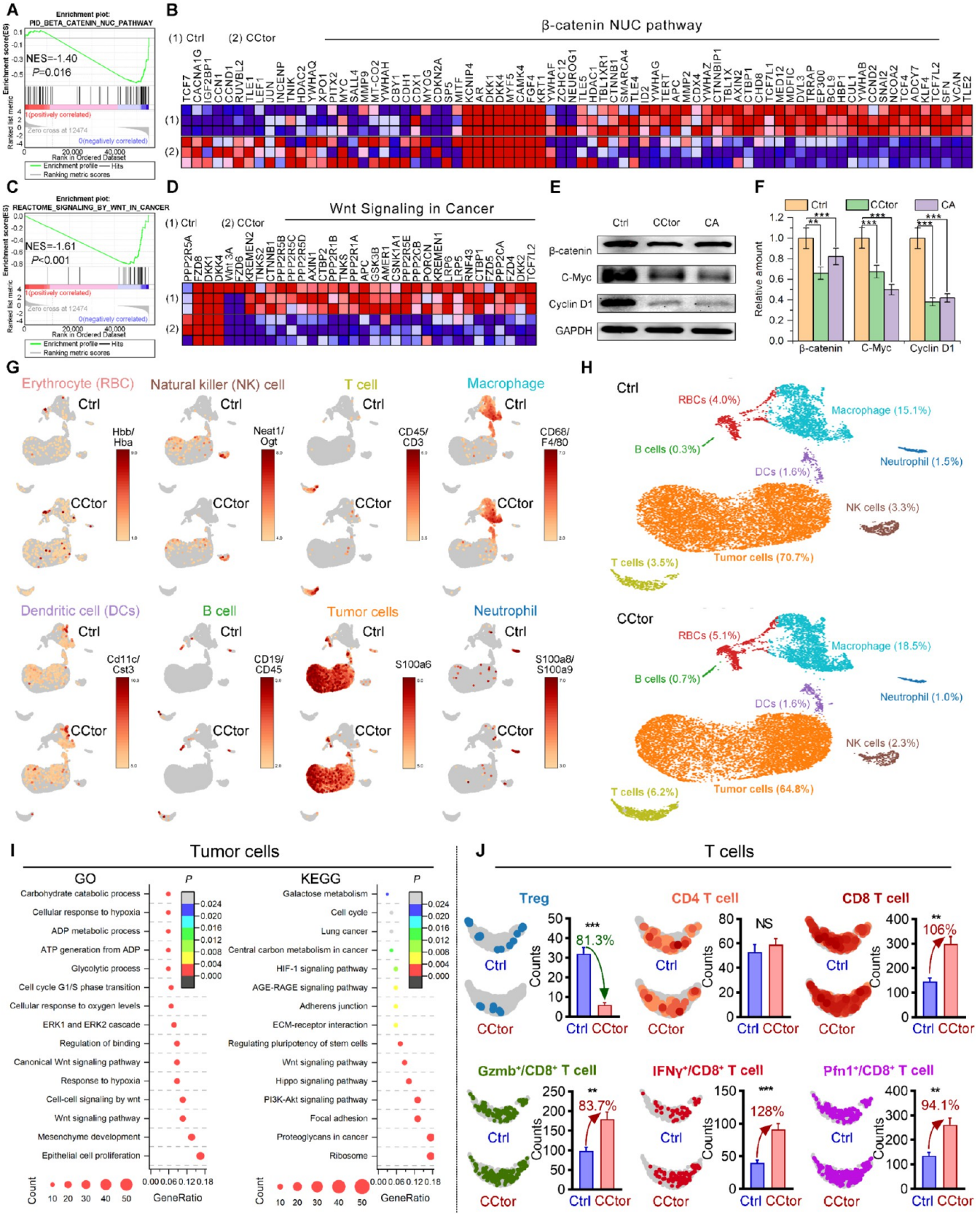

Figure 4. CCtor effectively inhibits intracellular Wnt/β-catenin signaling and synergizes immune sensitization in vivo. (A) Gene set enrichment analysis (GSEA) results β-catenin NUC pathway after CCtor treatment. (B) Heat map of different metabolites in β-catenin signaling NUC pathway by CCtor compared to control (n = 3). (C) Gene set enrichment analysis (GSEA) results Wnt signaling pathway in cancer treatment with CCtor. (D) Heat map of different metabolites in Wnt signaling pathway in cancer by CCtor compared to control (n = 3). (E) The protein expression of Wnt/β-catenin signaling pathway was assessed using Western blot in erlotinib-resistant PC-9 cell line with the 48 h treatments of control, CCtor, CA (n = 3). (F) The changes in β-catenin, CyclinD1 or C-Myc protein expression of were qualitatively analyzed using ImageJ (n

https://doi.org/10.1021/acsnano.4c14264
ACS Nano 2025, 19, 17273−17286

Figure 4. continued

= 3). *P* values were determined by student's *t* test: **, $p < 0.01$; ***, $p < 0.001$. (G) t-SNE plots showing the expression of selected marker genes in Erythrocyte (RBC), Natural killer (NK) cell, T cell, Macrophage, Dendritic cell (DCs), B cell, Tumor cells and Neutrophil. (H) Eight distinct subclusters: Erythrocyte (RBC), Natural killer (NK) cell, T cell, Macrophage, Dendritic cell (DCs), B cell, Tumor cells and Neutrophil. (I) GO and KEGG analysis of the up-regulated genes in tumor cells of ctrl in comparison to CCtor. (J)The counts of Treg, CD4 T cell, CD8 T cell, $Gzmb^+/CD8^+$ T cell, IFN-$\gamma^+/CD8^+$ T cell and PFN/CD8+ T cell, were quantitatively calculated comparing ctrl and CCtor group. *P* values were calculated by the independent sample *t* test.

immune checkpoint inhibitors on blocking the PD-1/PD-L1 interaction, we performed surface sealing of the PD-L1 antigen on tumor cells. As a result, the uptake of these particles by tumor cells was significantly reduced in the absence of the D-type PD-L1 antagonist peptide (PPI) (Figure S4B−C). These results support our initial hypothesis that PPI exerts its extracellular effects by binding to PD-L1. Subsequently, the ultraviolet−visible (UV−vis) absorption and FTIR spectra confirmed the formation of CCtor, showing higher typical absorption peaks of peptides and the characteristic peaks of both Ctor and CA (Figure 2C−D). HPLC analysis of the supernatant after centrifugation of the prepared CCtor solution indicated that 100% of Ctor and 92.1% of CA were assembled into the CCtor supramolecule (Figure S3B−C). Dynamic light scattering (DLS) and ζ-potential measurements under simulated tumor acidic microenvironment conditions showed a hydrated particle size of 280.2 nm and a ζ-potential of −20.1 mV for CCtor at pH 6.5 (Figure 2E,F). High-resolution-TEM (HRTEM) and energy-dispersive X-ray spectroscopy (EDS) analysis confirmed the uniform distribution of N, C, and O in the observed CCtor particles, consistent with their components (Figure S3D,E). These data indicate the successful construction of the protein-like polypeptide condensate CCtor. Furthermore, to evaluate the kinetic stability of CCtor upon entering the bloodstream, the particle size of CCtor was measured using dynamic light scattering (DLS) at 0, 24, 72, 96, 120, and 144 h in a PBS solution containing 20% serum (to mimic the in vivo environment) (Figures S5). Over the course of 1 week, the particle size remained approximately 280 nm, demonstrating excellent colloidal stability.

Pharmaceutical Characteristics of CCtor. To investigate the internalization feature of CCtor, FITC-labeled CCtor and Ctor (CA-free control) were employed to assess uptake by Jurkat (T cells), RAW264.7 (macrophage), and LLC cells (LUAD cells). As anticipated, both confocal microscopy and flow cytometry consistently demonstrated a greater uptake of CCtor in LLC cells compared to Jurkat and RAW264.7 cells (Figure 3A−C). In order to confirm the micropinocytosis-mediated internalization of CCtor into LLC, macropinocytosis inhibitors Amiloride and Cytochalasin D were preincubated with LLC, resulting in significant suppression of CCtor internalizations (Figure 3D).

Following internalization, FITC-labeled CCtor exhibited significant colocalization with the lysosome probe Lysotracker (Pearson coefficient 0.86), indicating that CCtor undergoes degradation within the lysosome and subsequently releases D-type PPI into the extracellular space (Figure 3E−H). Subsequent analysis confirmed the release of biotin-labeled PPI from LLC cells, with the highest biotin content observed at 12 h postinternalization (Figure 3I). Further investigation into PPI's role in PD-L1 degradation on the cell membrane revealed a substantial reduction in PD-L1 fluorescence on LLC cells treated with CCtor compared to controls (Figures S6A and S7A,B). These findings suggest that CCtor is internalized via macropinocytosis, undergoes lysosomal degradation, and releases PPI to degrade PD-L1, thereby restoring normalcy to the tumor immune microenvironment (Figure 3J).

Furthermore, due to the distinctive activation of micropinocytosis in tumors, CCtor is anticipated to exhibit remarkable tumor targeting capabilities. To validate this hypothesis, Cy5-labeled CCtor was synthesized and intravenously administered to C57BL/6 mice with subcutaneous LLC transplantation tumors. As anticipated, CCtor demonstrated maximum accumulation at the tumor sites compared to various other organs such as the heart, liver, spleen, lungs, and kidneys (Figure 3K−M), indicating a preferential profile for tumor accumulation.

CCtor Effectively Inhibits Wnt/β-Catenin Signaling and Enhances Immune Sensitization. CCtor significantly inhibited tumor cell proliferation at the cellular level, as evidenced by marked cell cycle arrest (Figure S8A−C). GSEA analysis of CCtor-treated cells showed significant downregulation of nuclear β-catenin and Wnt signaling pathways compared to controls (Figure 4A−D). Western blot analysis confirmed the significant downregulation of β-catenin and its downstream molecules C-myc and Cyclin D1 in CCtor-treated cells, with the most pronounced downregulation observed compared to CA-treated and control groups (Figures 4E,F and S9). The β-catenin was a critical component of the Wnt signaling pathway, and clinical data analysis revealed a positive correlation between β-catenin and PD-L1 expression. To further investigate whether CCtor regulates PD-L1 expression at the protein level, we conducted experiments on two distinct lung adenocarcinoma cell lines (Figure S10A,B). Western blot results demonstrated that CCtor downregulated PD-L1 expression at various time points. Notably, CA-induced downregulation of PD-L1 was significantly delayed compared to CCtor, suggesting that CA indirectly modulates PD-L1 expression via the Wnt/β-catenin pathway. In contrast, PPI, a D-type PD-L1 antagonist peptide within CCtor, directly interacts with PD-L1. In conclusion, the CCtor effectively suppressed the activation of the canonical Wnt/β-catenin signaling pathway and downregulated PD-L1 expression in tumor cells.

In vivo single-cell sequencing of LLC subcutaneous tumors identified various immune cells and a distinct tumor cell population (Figure 4G,H). GO and KEGG clustering of significantly downregulated genes in CCtor-treated tumor cells revealed suppression of aberrantly elevated Wnt signaling, energy metabolism, and cell cycle pathways (Figure 4I). T cell subpopulation analysis revealed a significant reduction in Treg cell markers and an elevation in cytotoxic T cell markers in CCtor-treated tumors, suggesting the normalization of the tumor-suppressive immune microenvironment (Figure 4J).

***In Vivo* Antitumor Efficacy of CCtor in C57 Mice Bearing LLC Tumors.** Given CCtor's significant tumor cell enrichment and Wnt/β-catenin signaling inhibition at the cellular level, its antitumor efficacy was evaluated in vivo using a C57 mouse subcutaneous LLC tumor model. Mice were

https://doi.org/10.1021/acsnano.4c14264
ACS Nano 2025, 19, 17273−17286

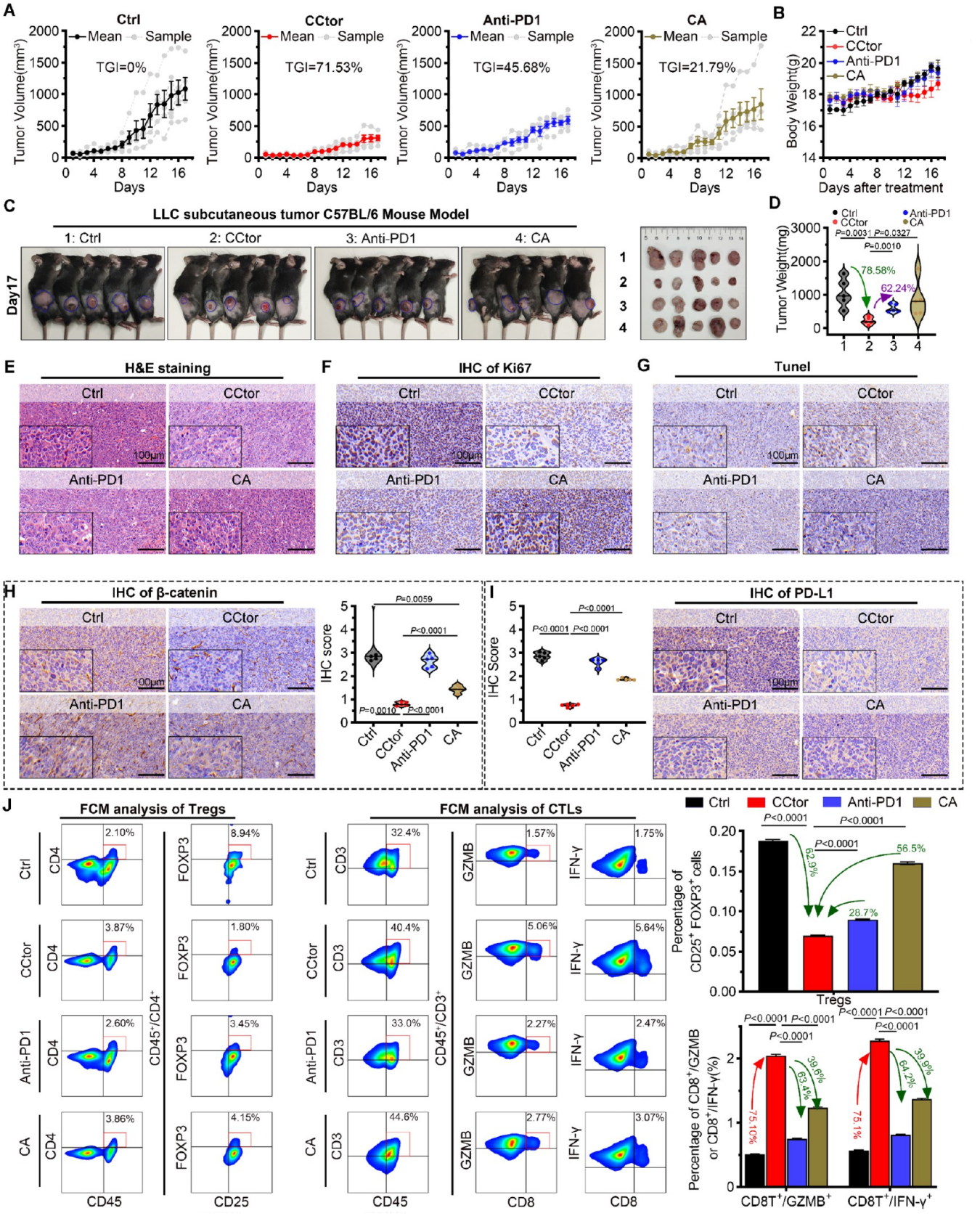

Figure 5. CCtor suppresses Wnt/β-catenin signaling and synergizes immune sensitization, together exerting excellent antitumor effects in C57BL/6 subcutaneous tumor model. (A) The tumor growth curves of LLC allograft tumors in C57BL/6 mice with PBS, CCtor, anti-PD1 and CA treatment, respectively (n = 5). (B) Changes in body weight were recorded during the period of indicated treatment (n = 5). (C) Photographs of C57BL/6 subcutaneous tumor model and ex-vivo tumor tissues (n = 5). (D) Tumor weights from C57 mice bearing LLC tumors with the PBS, CCtor, anti-PD1 and CA treatment, respectively (n = 5). (E-G) The representative images of H&E staining (E) and IHC of Ki67

https://doi.org/10.1021/acsnano.4c14264
ACS Nano 2025, 19, 17273−17286

Figure 5. continued

staining (F) and Tunel of LLC tumors with PBS, CCtor, anti-PD1 and CA treatment, respectively. (Scale bar: 100 μm). (H&I) The IHC staining of β-catenin(H) and PD-L1(I) in tumor sections from mice with the indicated treatments (scale bar: 100 μm). The IHC scores of β-catenin(H) and PD-L1(I) were plotted with violin plots (n = 5). (J) Representative flow cytometry displayed the proportions of Tregs and cytotoxic lymphocytes (CTLs) in C57BL/6 subcutaneous tumor with PBS, CCtor, anti-PD1 and CA treatment, respectively. Quantification analysis of $CD25^+$ $FOXP3^+$cells, $CD8^+$ $GZMB^+$, $CD8^+$ IFN-γ^+ in tumors tissue. P values were calculated by the independent sample t test.

treated with 2.5 mg/kg CCtor, PD-1 mAb, or CA for six sessions via tail vein injection, with tumor volumes measured daily. Tumor growth curves showed that CCtor significantly inhibited tumor growth compared to controls, with a TGI of 71.53%, outperforming PD-1 mAb (TGI < 50%) and CA (TGI < 30%) treatments (Figure 5A). Mice in the CCtor group-maintained weight gain throughout the treatment period, indicating no significant toxicity (Figure 5B). Photographs of mice and excised tumors post-treatment showed a 62.24% reduction in tumor weight in the CCtor group compared to the PD-1 mAb group and a 78.58% reduction compared to controls, corroborating the tumor growth inhibition results (Figure 5C−D). CCtor also significantly inhibited proliferation and promoted apoptosis in tumors compared to other treatments (Figure 5E−G). Mechanistic analysis revealed significant inhibition of β-catenin, Cyclin D1, and C-Myc expression in CCtor-treated tumors (Figures 5H and S11A,B), linking CCtor's antitumor effect to Wnt/β-catenin signaling inhibition. Analysis of PD-L1 expression in tumor tissues showed that CCtor significantly reduced PD-L1 expression, indicating enhanced antitumor immune sensitization compared to other treatments (Figure 5I). Furthermore, a pronounced decrease in TGF-β expression was detected in the CCtor treatment group (Figure SI2A). TGF-β and the Wnt signaling pathway are intricately interconnected, with each pathway modulating the activity of the other. CCtor likely disrupts the β-catenin/BCL9 interaction by interfering with the Wnt/β-catenin signaling pathway, thereby reducing TGF-β expression. Within the tumor microenvironment, TGF-β plays a crucial role in regulating the secretion of chemokines by both tumor cells and immune cells. CCL22 and CCL20, members of the CC chemokine subfamily, are key immunosuppressive chemokines involved in the recruitment of regulatory T cells to the tumor microenvironment. In the CCtor-treated tumors, the expression levels of CCL22 and CCL20 were markedly decreased, leading to reduced infiltration of immunosuppressive T cells into the tumor, thereby enhancing the therapeutic efficacy of CCtor. Mechanistically, CCtor inhibits the infiltration of regulatory Treg cells via the TGF-β-CCL20/CCL22 axis. Further analysis of Treg and CTL populations using multichannel FCM revealed a significant reduction in Treg cells and an increase in CD8T/Granzyme B and CD8T/IFN-γ populations in CCtor-treated tumors compared to PD-1 mAb-treated tumors (Figure 5J). These results demonstrate that CCtor inhibits tumor cell infiltration by Tregs, enhances CTL cytotoxicity, and exerts potent antitumor immune sensitization.

Potent Immunotherapy Efficacy of CCtor in a Mouse LUAD Orthotopic Model. The remarkable inhibition of subcutaneous tumors prompted the establishment of a more clinically relevant model for the tumor microenvironment. By establishing an orthotopic LUAD model in mice through tail vein injection, we evaluated the in vivo effects of CCtor (Figure 6A). Mice were treated with PBS (control), PD-1 mAb (2.5 mg/kg), or CCtor (2.5 mg/kg) every 3 days for 11 sessions (Figure 6A). Post-treatment, CCtor significantly reduced lung tumor nodules compared to controls and PD-1 mAb treatments, with significant differences in statistical analysis (Figure 6B−C). Histological analysis showed that CCtor alleviated lung fibrosis, reduced collagen fiber deposition, and decreased lesion areas compared to other treatments (Figure 6D,E). CCtor-treated mice exhibited a median survival time of 36.5 days, outperforming control (23 days) and PD-1 mAb (27.5 days) treatments (Figure 6F). Notably, PD-1 mAb treatment did not significantly differ from controls in tumor nodule number, tumor area, collagen deposition, or median survival, indicating resistance (Figure 6B−F). Tunel staining showed increased apoptosis in CCtor-treated tumors compared to controls (Figure S13A). Ki67 IHC staining indicated significant downregulation of proliferation in CCtor-treated tumors (Figure 6G). Overall, these results demonstrate that CCtor inhibits LUAD cell growth and effectively treats LUAD orthotopic tumors with superior antitumor efficacy compared to PD-1 mAb.

IHC analysis of lung tumor tissues revealed significant downregulation of β-catenin, Cyclin D1, C-Myc, and PD-L1 in CCtor-treated tumors compared to controls and PD-1 mAb-resistant groups, indicating effective inhibition of Wnt/β-catenin and PD-L1 pathways (Figure 6H−L). Consistent with the findings in subcutaneous tumor models, the CCtor treatment group exhibited markedly reduced expression of TGF-β, as well as significantly lower levels of the immunosuppressive chemokines CCL22 and CCL20 (Figure S14A). These observations suggest that CCtor inhibits the infiltration of regulatory Treg cells via the TGF-β-CCL20/CCL22 axis. Immune cell infiltration analysis showed a significant increase in CD3+/CD8+ T cells and a decrease in CD4+/CD25+ T cells in CCtor-treated tumors, confirming enhanced immune response (Figure 6M,N). These results suggest that CCtor effectively blocks Wnt/β-catenin and PD-1/PD-L1 pathways, enhancing tumor-specific immune responses and providing a promising antitumor strategy.

Biocompatibility and Safety of CCtor. To evaluate CCtor's biocompatibility, healthy C57BL/6 mice were injected with PBS (control) or CCtor (high dose 7.5 mg/kg, low dose 2.5 mg/kg) every other day for seven sessions. Weight monitoring revealed no significant differences between CCtor-treated and control groups, with continuous weight gain throughout the treatment period (Figure 7A). Hematological analysis revealed no significant adverse effects on WBC, RBC, LYMPH, or PLT in CCtor-treated groups (Figure 7B). Histopathological examination of organ slices post-treatment showed no significant changes in the morphology of vital organs, and liver and kidney function levels remained unchanged (Figure 7C−G). Biochemical analysis of immune-related toxicity indicators (TNF-α, IFN-γ, IL-1β, IL-4) in serum and organ tissues showed no immune-related adverse reactions (Figure 7H−L). These results demonstrate the excellent biocompatibility and safety of CCtor in vivo.

https://doi.org/10.1021/acsnano.4c14264
ACS Nano 2025, 19, 17273−17286

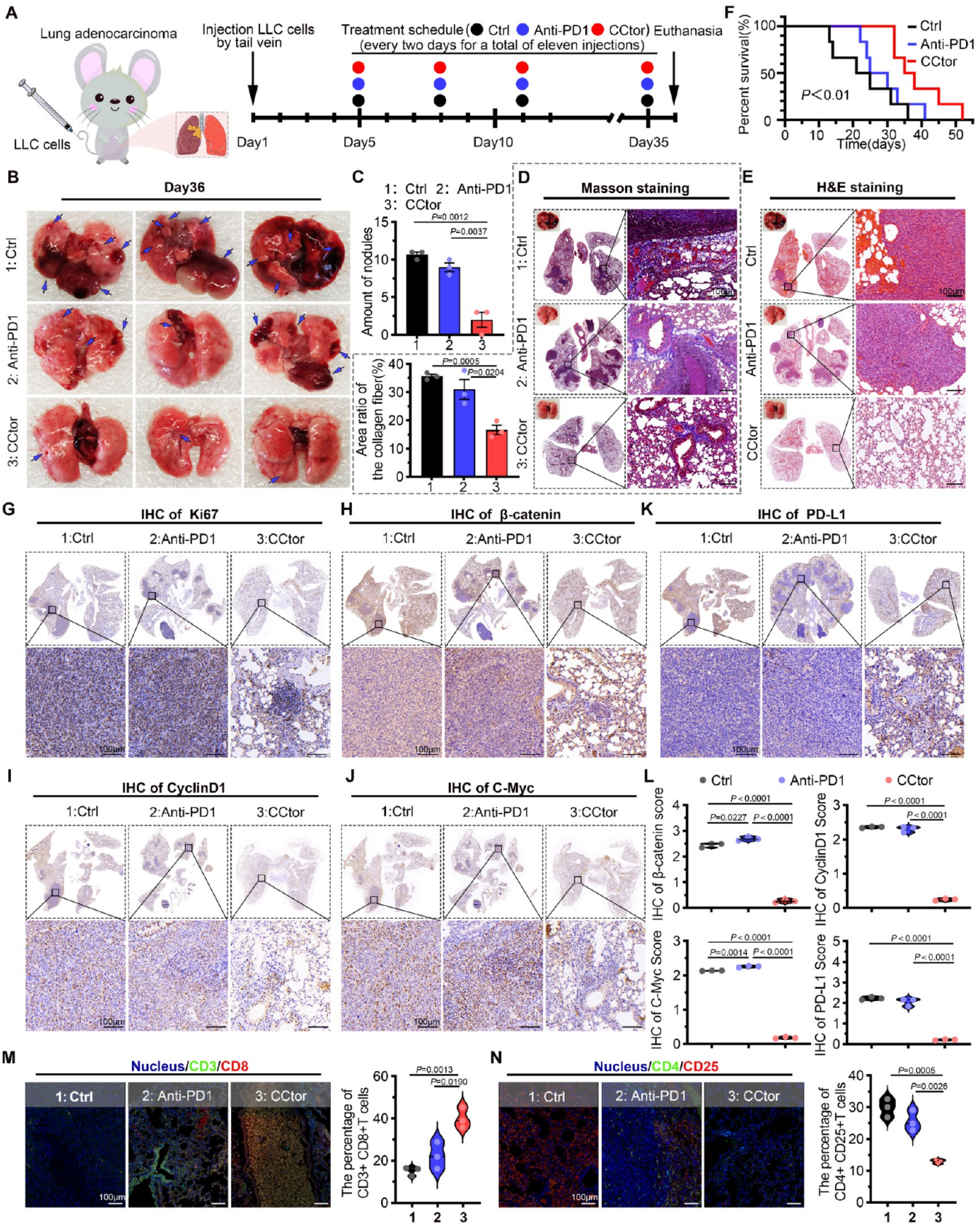

Figure 6. CCtor enhances immunotherapy in lung adenocarcinoma orthotopic allograft mice model. (A) Schematic depiction of lung adenocarcinoma orthotopic allograft model was established by tail-vein injection LLC cells. The therapeutic process of lung adenocarcinoma was implied with intravenous injection of CCtor, anti-PD, or PBS every 2 days for a total of 11 times. (B−C) The photographic images of lung tumors with indicated treatments at 36 days. The superficial macroscopic metastases in the lungs were marked with blue arrows (B). The number of lung tumor nodules per mouse with PBS, CCtor or CA treatment (C) (n = 3). (D) The Masson staining of lung tissues bearing

https://doi.org/10.1021/acsnano.4c14264
ACS Nano 2025, 19, 17273−17286

Figure 6. continued

tumors. (Scale bar: 100 μm). Quantification of collagen fiber area (n = 3). (E) The H&E staining of lung tissues bearing tumors. (Scale bar: 100 μm). (F) Survival curves of mice with LLC lung tumors and treated with CCtor, Anti-PD1, or PBS intravenous injection. *P* values were calculated by the Log-rank test. (G−K) Representative IHC staining of Ki67(G), β-catenin(H), CyclinD1(I), C-Myc (J) and PD-L1 (K) for lung tumors after drug treatments for 36 days. (Scale bar: 100 μm). (L) The IHC scores of β-catenin, CyclinD1, C-Myc and PD-L1 were plotted with violin plots (n = 3). (M, N) Immunofluorescence images of $CD3^+/CD8^+$ cells (M) and $CD4^+/CD25^+$ cells (N) in lung tumor sections with various drug treatments. (Scale bar: 100 μm). The percentage of $CD3^+/CD8^+$ cells and $CD4^+/CD25^+$ cells were presented as mean ± s.d. 1, Ctrl group; 2, Anti-PD1(2.5 mg/kg) group;3, CCtor (2.5 mg/kg) group. *P* values were calculated the independent sample by *t*-test.

STUDY LIMITATIONS

The present study, while demonstrating promising results in the development of CCtor as a potential therapeutic candidate for nonsmall cell lung cancer (LUAD), inevitably entails certain limitations that necessitate careful consideration. These limitations are pivotal to comprehending the broader implications and future directions of this research.

First, despite its significant promise regarding targeting specificity, delivery efficiency, and therapeutic efficacy, CCtor is currently produced via laboratory-scale synthesis. This production method presents several challenges that must be resolved before large-scale manufacturing and industrialization can be realized. A critical issue is the inherent absence of stringent quality control measures at the laboratory level. Unlike industrial processes, which typically incorporate rigorous standards and automated systems to ensure consistency, laboratory-scale synthesis may lack the same level of precision and reproducibility. Moreover, the generally high production costs associated with laboratory-scale synthesis pose an additional substantial challenge. Achieving scalable production will require innovative strategies to reduce costs while preserving the quality and efficacy of CCtor.

Second, the experimental validation of CCtor's ability to target the Wnt/β-catenin signaling pathway and exhibit robust antitumor effects has predominantly relied on in vivo and ex vivo models. While these models have provided valuable insights into the mechanisms and efficacy of CCtor, they cannot fully emulate the complexity of clinical tumor characteristics. Tumors in real-world clinical settings are influenced by numerous factors, including genetic heterogeneity, microenvironmental interactions, and patient-specific variables such as age, comorbidities, and treatment history. Although animal models are essential tools in preclinical research, they may not fully capture all these intricacies. For instance, the immune response observed in animal models might differ significantly from that in humans, potentially impacting the translatability of findings.

To bridge the gap between preclinical studies and clinical applications, further comprehensive investigations are warranted. Advanced modeling techniques, such as 3D tumor spheroids, organoids, and patient-derived xenografts (PDX), provide promising alternatives to traditional animal models. These models more accurately replicate the physiological and pathological conditions of human tumors, offering a more reliable platform for assessing the efficacy and safety of therapeutic candidates like CCtor. Integrating these advanced models into future studies will deepen our understanding of CCtor's therapeutic potential and expedite its clinical translation.

Looking ahead, the investigation of CCtor's therapeutic potential will persist within the frameworks of preclinical and translational research. This entails not only refining the production process and addressing the aforementioned limitations but also broadening the scope of inquiry to encompass diverse patient populations and tumor types. By doing so, researchers aim to construct a holistic profile of CCtor's efficacy, safety, and applicability across various clinical contexts. Ultimately, these endeavors will advance the field of cancer therapy and enhance outcomes for patients with nonsmall cell lung cancer and potentially other malignancies.

CONCLUSIONS

This study utilized clinical data from nonsmall cell lung cancer (LUAD) to identify the activation of Wnt/β-catenin signaling, PD-1 signaling, and macropinocytosis pathways as significant distinguishing features of tumor tissues. Researchers designed a coassembled intermediate peptide of CA and a PD-L1 blocking peptide, constructing a self-assembled protein-like polypeptide condensate CCtor using a robust method. CCtor utilizes tumor cell macropinocytosis for internalization and lysosomal degradation for drug release, achieving dual inhibition of Wnt/β-catenin and PD-L1 pathways. CCtor specifically targets tumor cells in the tumor microenvironment, exhibits excellent biocompatibility, and shows no immune-related toxicity in vivo. Subcutaneous and orthotopic tumor models demonstrated that CCtor, as an immune checkpoint inhibitor, has superior antitumor effects compared to anti-PD-1 monotherapy. Collectively, the significance of this study surpasses its immediate clinical implications, as it establishes a comprehensive model for tumor normalization therapy that seamlessly integrates AI-driven identification of critical aberrant signaling pathways with targeted interventions to rectify these abnormalities. This groundbreaking model heralds a paradigm shift in cancer treatment, offering an avenue to achieve tumor normalization and enhance patient outcomes through the meticulous fusion of advanced computational techniques and innovative therapeutic design.

METHODS/EXPERIMENTAL SECTION

General Remarks. All chemical reagents for this research were supplied by Sigma-Aldrich. All commercial products were directly used without additional purification.

Synthesis of Ctor. The Ctor peptide was synthesized on a CS bio 336X automated peptide synthesizer using an HBTU activation/DIEA in situ neutralization procedure optimized on a suitable resin based on Fmoc chemical SPPS. After cleavage and deprotection in a reagent cocktail containing 88% TFA, 5% phenol, 5% H_2O, and 2% TIPS, it was precipitated with cold ether and purified to homogeneity by preparative C18 reversed-phase HPLC. The relative molecular masses of synthetic Ctor were detected by electrospray ionization mass spectrometry (ESI-MS).

Preparation of CCtor. The previously lyophilized Ctor powders were dispersed into distilled water at room temperature at the final concentration of (1 mg/mL). Subsequently, 0.5, 1, 2 mg CA was respectively dissolved in DMSO, which were dropwise added to the above Ctor solution and ultrasonicated for reaction 10 min, resulting in a milk white solution, namely CCtor.

Physicochemical Characterization of CCtor. The prepared series of CCtor solutions (the mass ratios of Ctor/CA respectively were

https://doi.org/10.1021/acsnano.4c14264
ACS Nano 2025, 19, 17273−17286

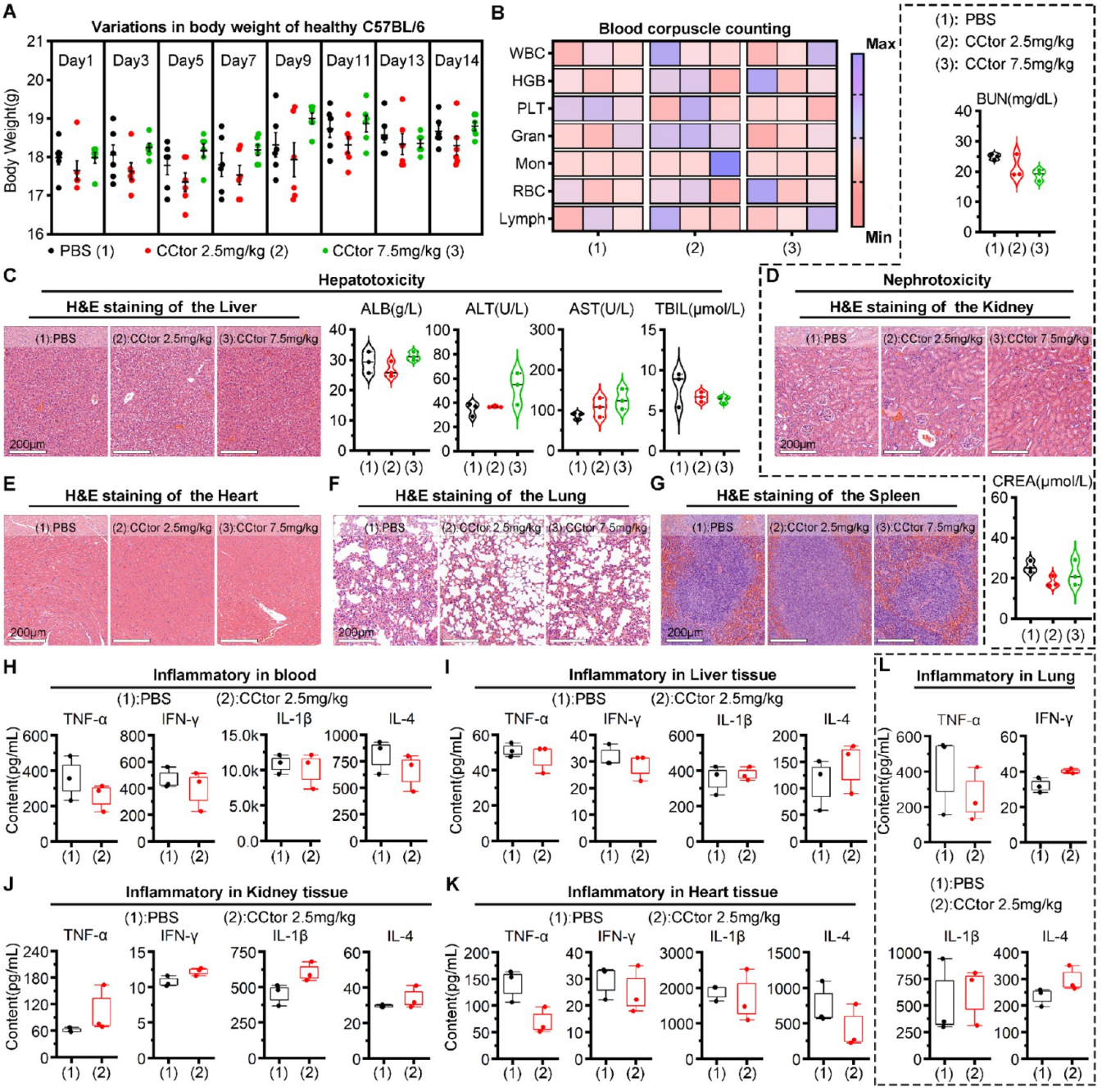

Figure 7. CCtor have a favorable biosafety profile and mitigate the incidence of immune-related adverse events (IrAEs) in vivo. (A) The body weight variations of healthy C57BL/6 upon indicated treatments every other day ($n = 6$). (B) Blood corpuscle counting of the CCtor group and PBS group were drawn with a heatmap. WBC, white blood cell; HGB, hemoglobin; PLT, Platelets; Gran, granulocytes; Mon, monocytes; RBC, red blood cell; Lymph, lymphocyte. (1): PBS; (2): CCtor 2.5 mg/kg; (3): CCtor 7.5 mg/kg. These above data are standardized as z-score ($n = 3$). (C) Hepatotoxicity testing of treatment with CCtor measured by pathological section of the liver (scale bar: 200 μm), liver function (ALB, ALT, AST, and TBIL) ALB, albumin; ALT, aspartate transaminase; AST, alanine aminotransferase; TBIL, total bilirubin. (1): ctrl; (2): CCtor 2.5 mg/kg; (3): CCtor 7.5 mg/kg. ($n = 3$). (D) Nephrotoxicity testing of treatment with CCtor measured by pathological section of the kidney (scale bar: 200 μm), kidney function (BUN and CREA) ($n = 3$). (E–G) The testing of heart (E), pulmonary (F) and spleen (G) toxicity was detected by the pathological section of the heart, lung and spleen (scale bar: 200 μm). (H–L) IrAEs of CCtor was assessed by detecting inflammatory marks (TNF-α, IFN-γ, IL-1β, and IL-4) in blood (H), liver tissues (I), kidney tissues (J), heart tissue (K) and lung tissues (L). (1): PBS group; (2): CCtor 2.5 mg/kg group ($n = 3$).

1:0.5, 1:1, and 1:2) were dripped onto the carbon-coated copper, and then the shape and size of CCtor particles were recorded at an acceleration voltage of 120 kV by Transmission Electron Microscope (Talos L 120C G2, Thermo Fisher Scientific). The morphology and energy-dispersive spectroscopy (EDS) analysis were observed by Lorenz transmission electron microscopy (Talos F200X, Thermo Fisher Scientific). The hydrodynamic size distribution and ζ-potential of the CCtor (with a mass ratio of Ctor/CA = 1:1, 1 mL) were characterized using dynamic light scattering (DLS). The modified surface chemical structure of CCtor was determined by Fourier Transform Infrared Spectroscopy (FTIR) and UV–vis Spectroscopy. In addition, the proportion of Ctor and CA loaded on CCtor was

https://doi.org/10.1021/acsnano.4c14264
ACS Nano 2025, 19, 17273–17286

measured by high performance liquid chromatography (HPLC). Specifically, CCtor solution was centrifuged at 5000 rpm for 5 min to obtain supernatant, which then assayed for the amount of free Ctor and CA by HPLC.

ASSOCIATED CONTENT

Supporting Information

The Supporting Information is available free of charge at https://pubs.acs.org/doi/10.1021/acsnano.4c14264.

Detailed descriptions of reagents, rigorous protocols for evaluating the in vitro stability and in vivo activity of CCtor, systematic procedures for constructing animal-based LLC tumor xenograft models and orthotopic lung adenocarcinoma mouse models, and essential experimental guidelines, and statistical analyses, along with 14 figures (PDF)

AUTHOR INFORMATION

Corresponding Authors

Wangxiao He − *Department of Medical Oncology and Department of Talent Highland, The First Affiliated Hospital of Xi'an Jiaotong University, Xi'an 710061, P. R. China;* orcid.org/0000-0002-2054-6022; Email: hewangxiao5366@xjtu.edu.cn

Jin Yan − *Department of Infectious Diseases and Hepatology and National & Local Joint Engineering Research Center of Biodiagnosis and Biotherapy, The Second Affiliated Hospital of Xi'an Jiaotong University, Xi'an 710004, P. R. China;* orcid.org/0000-0001-6468-6003; Email: yanjin19920602@xjtu.edu.cn

Yanmin Zhang − *Department of Infectious Diseases and Hepatology, The Second Affiliated Hospital of Xi'an Jiaotong University, Xi'an 710004, P. R. China; State Key Laboratory of Shaanxi for Natural Medicines Research and Engineering, Xi'an 710061, P. R. China; School of Pharmacy, Health Science Center, Xi'an Jiaotong University, Xi'an 710061, P. R. China;* orcid.org/0000-0001-7307-9408; Email: zhang2008@xjtu.edu.cn

Authors

Jingmei Wang − *Department of Infectious Diseases and Hepatology and Institute for Stem Cell & Regenerative Medicine, The Second Affiliated Hospital of Xi'an Jiaotong University, Xi'an 710004, P. R. China*

Weiming You − *Department of Infectious Diseases and Hepatology, The Second Affiliated Hospital of Xi'an Jiaotong University, Xi'an 710004, P. R. China; State Key Laboratory of Shaanxi for Natural Medicines Research and Engineering, Xi'an 710061, P. R. China*

Complete contact information is available at: https://pubs.acs.org/10.1021/acsnano.4c14264

Author Contributions

[▽]W.H., J.Y., and Y.Z. contributed equally to this work.

Notes

The authors declare no competing financial interest.

ACKNOWLEDGMENTS

This work was supported by The National Key Research and Development Program of China (No. 2022YFE0133500), The National Natural Science Foundation of China (Nos. 22007076, 82272782, 32171256), Thousand Talents Plan of Shaanxi Province (For W.H.), The Key R&D plan of Shaanxi Province (No. 2023-YBSF-098), "The Young Talent Support Plan" of Xi'an Jiaotong University (W.H.), "Young doctor training program" of Xi Jing Hospital (J.Y.). We thank Instrument Analysis Center of Xi'an Jiaotong University for their assistance with TEM analysis. We extend our heartfelt gratitude to the Home for Researchers (www.home-for-researchers.com) for their meticulous work in color-matching the Figure 2A and Toc graphic.

REFERENCES

(1) Flores, E. R.; Sawyer, W. G. Engineering cancer end: An interdisciplinary approach to confront the complexities of cancer. *Cancer Cell* **2024**, *42* (7), 1133−1137.

(2) Hanahan, D.; Weinberg, R. A. Hallmarks of cancer: the next generation. *Cell* **2011**, *144* (5), 646−674.

(3) Junttila, M. R.; de Sauvage, F. J. Influence of tumour microenvironment heterogeneity on therapeutic response. *Nature* **2013**, *501* (7467), 346−354.

(4) de Visser, K. E.; Joyce, J. A. The evolving tumor microenvironment: From cancer initiation to metastatic outgrowth. *Cancer Cell* **2023**, *41* (3), 374−403.

(5) Peters, G. W.; Hallemeier, C. L.; Jethwa, K. R. Time to reconsider staging laparoscopy in pancreatic cancer? *J. Clin. Oncol.* **2020**, *38* (25), 2944−2945.

(6) Mortezaee, K. Normalization in tumor ecosystem: Opportunities and challenges. *Cell Biol. Int.* **2021**, *45* (10), 2017−2030.

(7) Martin, J. D.; Seano, G.; Jain, R. K. Normalizing Function of Tumor Vessels: Progress, Opportunities, and Challenges. *Annu. Rev. Physiol.* **2019**, *81*, 505−534.

(8) Hanahan, D.; Coussens, L. M. Accessories to the Crime: Functions of Cells Recruited to the Tumor Microenvironment. *Cancer Cell* **2012**, *21* (3), 309−322.

(9) Mueller, M. M.; Fusenig, N. E. Friends or foes — bipolar effects of the tumour stroma in cancer. *Nat. Rev. Cancer* **2004**, *4* (11), 839−849.

(10) Mpekris, F.; Voutouri, C.; Baish, J. W.; Duda, D. G.; Munn, L. L.; Stylianopoulos, T.; Jain, R. K. Combining microenvironment normalization strategies to improve cancer immunotherapy. *Proc. Natl. Acad. Sci. U.S.A.* **2020**, *117* (7), 3728−3737.

(11) Choi, E. J.; Lee, J. H.; Park, H. S.; Lee, J. H.; Seol, M.; Lee, Y. S.; Kang, Y. A.; Jeon, M.; Woo, J. M.; Kang, H.; Lee, K. Androgen therapy for patients with lower-risk myelodysplastic syndrome and significant cytopenia: a retrospective study. *Br. J. Hamaetol.* **2019**, *187* (1), e4−e7.

(12) Lane, A. A.; Chabner, B. A. Histone Deacetylase Inhibitors in Cancer Therapy. *J. Clin. Oncol.* **2009**, *27* (32), 5459−5468.

(13) Tsimberidou, A. M.; Fountzilas, E.; Nikanjam, M.; Kurzrock, R. Review of precision cancer medicine: Evolution of the treatment paradigm. *Cancer Treat. Rev.* **2020**, *86*, No. 102019.

(14) de Thé, H. Differentiation therapy revisited. *Nat. Rev. Cancer* **2018**, *18* (2), 117−127.

(15) Downward, J. Targeting RAS signalling pathways in cancer therapy. *Nat. Rev. Cancer* **2003**, *3* (1), 11−22.

(16) You, M.; Xie, Z.; Zhang, N.; Zhang, Y.; Xiao, D.; Liu, S.; Zhuang, W.; Li, L.; Tao, Y. Signaling pathways in cancer metabolism: mechanisms and therapeutic targets. *Signal Transduction Targeted Ther.* **2023**, *8* (1), No. 196.

(17) Yang, L.; Shi, P.; Zhao, G.; Xu, J.; Peng, W.; Zhang, J.; Zhang, G.; Wang, X.; Dong, Z.; Chen, F.; Cui, H. Targeting cancer stem cell pathways for cancer therapy. *Signal Transduction Targeted Ther.* **2020**, *5* (1), No. 8.

(18) Yang, Y.; Li, X.; Wang, T.; Guo, Q.; Xi, T.; Zheng, L. Emerging agents that target signaling pathways in cancer stem cells. *J. Hematol. Oncol.* **2020**, *13* (1), No. 60.

(19) Levine, A. J.; Puzio-Kuter, A. M. The Control of the Metabolic Switch in Cancers by Oncogenes and Tumor Suppressor Genes. *Science* **2010**, *330* (6009), 1340−1344.

(20) Liu, Y.; Gu, W. The complexity of p53-mediated metabolic regulation in tumor suppression. *Semin. Cancer Biol.* **2022**, *85*, 4−32.

(21) Dong, Y.; Tu, R.; Liu, H.; Qing, G. Regulation of cancer cell metabolism: oncogenic MYC in the driver's seat. *Signal Transduction Targeted Ther.* **2020**, *5* (1), No. 124.
(22) Chaffer, C. L.; Weinberg, R. A. A Perspective on Cancer Cell Metastasis. *Science* **2011**, *331* (6024), 1559−1564.
(23) Pao, W.; Girard, N. New driver mutations in non-small-cell lung cancer. *Lancet Oncol.* **2011**, *12* (2), 175−180.
(24) Sboner, A.; Mu, X. J.; Greenbaum, D.; Auerbach, R. K.; Gerstein, M. B. The real cost of sequencing: higher than you think! *Genome Biol.* **2011**, *12* (8), No. 125.
(25) Mardis, E. R. Next-Generation Sequencing Platforms. *Annu. Rev. Anal. Chem.* **2013**, *6*, 287−303.
(26) Topol, E. J. High-performance medicine: the convergence of human and artificial intelligence. *Nat. Med.* **2019**, *25* (1), 44−56.
(27) Papachristou, I.; Bosanquet, N. Improving the prevention and diagnosis of melanoma on a national scale: A comparative study of performance in the United Kingdom and Australia. *J. Public Health Policy* **2020**, *41* (1), 28−38.
(28) Hänzelmann, S.; Castelo, R.; Guinney, J. GSVA: gene set variation analysis for microarray and RNA-Seq data. *BMC Bioinf.* **2013**, *14* (1), No. 7.
(29) Finotello, F.; Trajanoski, Z. Quantifying tumor-infiltrating immune cells from transcriptomics data. *Cancer Immunol., Immunother.* **2018**, *67* (7), 1031−1040.

https://doi.org/10.1021/acsnano.4c14264
ACS Nano 2025, 19, 17273−17286